INTERNATIONAL JOURNAL FOR NUMERICAL METHODS IN FLUIDS
Int. J. Numer. Meth. Fluids **28**: 73–94 (1998)

IMPLICIT UNFACTORED IMPLEMENTATION OF TWO-EQUATION TURBULENCE MODELS IN COMPRESSIBLE NAVIER–STOKES METHODS

G. BARAKOS AND D. DRIKAKIS*

UMIST, Department of Mechanical Engineering, PO Box 88, Manchester M60 1QD, UK

SUMMARY

An implicit unfactored method for the coupled solution of the compressible Navier–Stokes equations with two-equation turbulence models is presented. Both fluid-flow and turbulence transport equations are discretized by a characteristics-based scheme. The implicit unfactored method combines Newton subiterations and point-by-point Gauss–Seidel subrelaxation. Implicit-coupled and -decoupled strategies are compared for their efficiency in the solution of the Navier–Stokes equations in conjunction with low-*Re* two-equation turbulence models. Computations have been carried out for the flow over an axisymmetric bump using the $k-\epsilon$ and $k-\omega$ models. Comparisons have been obtained with experimental data and other numerical solutions. The present study reveals that the implicit unfactored implementation of the two-equation turbulence models reduces the computing time and improves the robustness of the CFD code in turbulent compressible flows. © 1998 John Wiley & Sons, Ltd.

KEY WORDS: compressible turbulent flows; implicit solver; characteristics-based method; low-*Re* two-equation turbulence models

1. INTRODUCTION

Development of new accurate and efficient CFD solvers for turbulent compressible flows is a subject of continuous interest. Even though many years of extensive research has been performed to develop new Navier–Stokes solvers, the computation of turbulent flows still remains a challenging problem. Inaccurate solutions of turbulent flows are due to turbulence modeling issues, but lack of robustness is mainly due to their numerical implementation.

In the past, algebraic turbulence models have been used as a quick way to extend a code from laminar to turbulent flows. Use of these models has been motivated by their simplicity and marginal numerical stiffness. However, experience has shown that in most cases, such crude modeling of turbulence did not provide satisfactory results. Most of the problems arise due to the local formulation of the models that neglects memory effects and the ambiguity to determine length scales of complex flows. Low-*Re* two-equation models seem to offer the best balance between accuracy and computational cost. The $k-\epsilon$ model [1,2] is one of the most popular two-equation turbulence models and in the past, the model has been used in conjunction with wall-functions for a variety of flows [1,3–5]. However, the model exhibits numerical stiffness and inaccuracies when applied to near-wall turbulent flows as well as

* Correspondence to: UMIST, Department of Mechanical Engineering, PO Box 88, Manchester M60 1QD, UK.

CCC 0271–2091/98/110073–22$17.50

Received August 1996
Revised July 1997

separated flows [3]. Various versions of the k–ϵ model have been proposed in order to improve the accuracy of the model in various flow cases [3–5]. An alternative to the k–ϵ model, which has also received considerable attention, is the k–ω model by Wilcox [6,7]. In the past, this model has been implemented in several flow cases by other authors [8,9].

The lack of numerical stability and robustness of low-*Re* number turbulence models is due, most of the time, to their numerical implementation. This numerical stiffness is also one of the main reasons for sometimes retracting the use of such models in an industrial environment. In the case of two-equation models, the turbulent kinetic energy is introduced in the Navier–Stokes equations and this has to be accounted for in the total energy budget. This may have no effect on the accuracy of the numerical solution, especially in subsonic and transonic flows, but it contributes to the Jacobian and eigenvector elements of the matrices in the implicit part of the equations. Further implications also arise from the treatment of the non-conservative source terms that dominate the formulation of all two-equation turbulence models. Most researchers implement low-*Re* turbulence models in a decoupled manner, according to which, the Navier–Stokes equations are firstly solved, and then the two turbulence equations are sequentially integrated in order to update the turbulent eddy viscosity [10–12]. Such procedures have been extensively used due to the little effort required to implement turbulence models into Navier–Stokes solvers; resulting, however, in slow numerical convergence. This deficiency is more severe when finer grids in the near-wall region are used.

Recently, the implicit-coupled solutions of the turbulence models and Navier–Stokes equations have attracted the interest of the CFD community [13,14]. Gerolymos and Vallet [13] have implicitly implemented the Launder–Sharma k–ϵ model using a fully coupled, approximately factored, implicit backward Euler method. They applied the method for a transonic flow with shock–boundary layer interaction and found that the method was robust and stable for Courant–Friedrichs–Lewy (CFL) numbers up to 50. Lin *et al*. [14] also presented an implicit-coupled solution of the Navier–Stokes equations in conjunction with Chien's k–ϵ model using a biconjugate gradient method with a preconditioner of incomplete lower-upper factorization. The conclusion of their study was that the biconjugate gradient (Bi-CGSTAB) method was more efficient than other variants of the Bi-CG method.

Implicit unfactored methods [15] based on Newton subiterations and Gauss–Seidel relaxation (IUNGS) have not yet been extended to turbulent flows coupled with low-*Re* two-equation models. IUNGS methods have so far been used for Euler [15,16] or Navier–Stokes simulations in conjunction with algebraic turbulence models [17–19]. In these studies, it has been shown that high CFL numbers can be obtained by IUNGS methods, while the numerical solution is less sensitive to the choice of the time step than the approximate factorization methods. Moreover, past studies [17,18,20] have shown that the combination of IUNGS with characteristics-based methods results in efficient CFD codes for both serial and parallel computations [21,22]. Therefore, the extension of IUNGS methods to turbulent flows in conjunction with low-*Re* two-equation models is worth investigating and this is the aim of the present study.

The objectives of this work are: (i) to extend an implicit unfactored method to the solution of the Navier–Stokes coupled with two-equation models (henceforth labeled implicit-coupled); (ii) to develop a characteristics-based discretization (Riemann solver) for the inviscid terms of the coupled system of equations; (iii) to investigate the efficiency of the implicit-coupled method in contrast to other numerical approaches based on the decoupled solutions of the fluid flow and turbulence equations; (iv) to implement all the above for the k–ϵ and k–ω models and to present comparisons for the solutions against experimental and numerical results from the literature. The paper is organised as follows: in Section 2 the governing

equations, turbulence models, characteristics-based method and implicit unfactored scheme are presented; in Section 3 the results of the present study are presented for a transonic flow case with shock/boundary layer interaction induced separation; finally, in Section 4, conclusions from the present work are drawn.

2. MATHEMATICAL MODELING

2.1. Governing equations

The compressible Navier–Stokes equations in conjunction with the differential equations for the two-equation turbulence model have been employed. The system of equations in curvilinear co-ordinates is written as

$$\frac{\partial U}{\partial t}+\frac{\partial E}{\partial \xi}+\frac{\partial G}{\partial \zeta}=\frac{\partial R}{\partial \xi}+\frac{\partial S}{\partial \zeta}+H_\phi+H_A, \tag{1}$$

where U is the six-component vector of the conservative variables

$$U=J(\rho, \rho u, \rho w, e, \rho k, \rho \phi)^T, \tag{2}$$

where ρ is the density; u and w are the velocity components in the x- and z-directions, respectively; e is the total energy of the fluid per unit volume and k is the turbulent kinetic energy. The variable ϕ denotes the isotropic turbulent dissipation, $\tilde{\epsilon}$, or the specific turbulence dissipation rate, ω, if the k–ϵ or the k–ω model is employed, respectively.

The inviscid (E, G) and viscous (R, S) fluxes are written as

$$\begin{aligned} E&=J(\tilde{E}\xi_x+\tilde{G}\xi_z), \quad G=J(\tilde{E}\zeta_x+\tilde{G}\zeta_z),\\ R&=J(\tilde{R}\xi_x+\tilde{S}\xi_z), \quad S=J(\tilde{R}\zeta_x+\tilde{S}\zeta_z), \end{aligned} \tag{3}$$

where the fluxes with a 'tilde' refer to the Cartesian co-ordinate system. The inviscid flux vectors, $\tilde{E}$ and $\tilde{G}$, and the viscous flux vectors, $\tilde{R}$ and $\tilde{S}$, are given by

$$\tilde{E}=\begin{pmatrix} \rho u \\ \rho u^2+p \\ \rho uw \\ (e+p)u \\ \rho uk \\ \rho u\phi \end{pmatrix}, \quad \tilde{G}=\begin{pmatrix} \rho w \\ \rho uw \\ \rho w^2+p \\ (e+p)w \\ \rho wk \\ \rho w\phi \end{pmatrix}, \tag{4}$$

$$\tilde{R}=\begin{pmatrix} 0 \\ t_{xx} \\ t_{xz} \\ ut_{xx}+wt_{xz}-\dot{q}_x \\ \left(\mu+\dfrac{\mu_t}{\sigma_k}\right)\dfrac{\partial k}{\partial x} \\ \left(\mu+\dfrac{\mu_t}{\sigma_\phi}\right)\dfrac{\partial \phi}{\partial x} \end{pmatrix}, \quad \tilde{S}=\begin{pmatrix} 0 \\ t_{zx} \\ t_{zz} \\ ut_{xz}+wt_{zz}-\dot{q}_z \\ \left(\mu+\dfrac{\mu_t}{\sigma_k}\right)\dfrac{\partial k}{\partial z} \\ \left(\mu+\dfrac{\mu_t}{\sigma_\phi}\right)\dfrac{\partial \phi}{\partial z} \end{pmatrix}. \tag{5}$$

The source term, H_A, accounts for axisymmetric flow problems [23] and is given in Section 2.5, while the source terms, H_ϕ, for the k–ϵ and k–ω turbulence models are given in Section 2.2.

The total energy per unit volume e includes the specific internal energy i, the kinetic energy of the fluid as well as the turbulent kinetic energy k

$$e = \rho i + \frac{1}{2}\rho(u^2 + w^2) + \rho k. \tag{6}$$

The pressure, p, is calculated by the perfect gas equation of state, $p = \rho\gamma i$, where γ is the ratio of specific heats, while the heat fluxes, $\dot{q}_i$, have been modeled according to Fourier's law.

In turbulent flows, the stress tensor t_{ij} is obtained by the sum of the viscous ($\bar{t}_{ij}$) and Reynolds stresses (τ_{ij}^R)

$$t_{ij} = \bar{t}_{ij} + \tau_{ij}^R. \tag{7}$$

Within the framework of linear eddy viscosity models, the Boussinesq approximation is used to calculate the Reynolds stresses.

2.2. Turbulence modeling

Low-*Re* eddy viscosity models include extra source terms, as well as damping functions and closure coefficients. The source term for the Launder–Sharma version [4] of the k–ϵ model is written as

$$H_\epsilon = J \begin{pmatrix} 0 \\ 0 \\ 0 \\ 0 \\ \tau_{ij}^R \dfrac{\partial u_i}{\partial x_j} - \rho\epsilon \\ C_{\epsilon_1} f_1 \dfrac{\tilde{\epsilon}}{k} \tau_{ij}^R \dfrac{\partial u_i}{\partial x_j} - C_{\epsilon_2} f_2 \rho \dfrac{\tilde{\epsilon}^2}{k} + \rho E \end{pmatrix}, \tag{8}$$

where the production term is given by

$$\tau_{ij}^R \frac{\partial u_i}{\partial x_j} = \mu_t \left[-\frac{2}{3}\left(\frac{\partial u_k}{\partial x_k}\right)^2 + \frac{1}{2}\left(\frac{\partial u_j}{\partial x_i} + \frac{\partial u_i}{\partial x_j}\right)^2 \right] - \frac{2}{3}\rho k \frac{\partial u_i}{\partial x_k}, \tag{9}$$

and the terms ϵ and E are defined as

$$\epsilon = \epsilon_0 + \tilde{\epsilon}, \quad \epsilon_0 = 2\frac{\mu}{\rho}\left(\frac{\partial\sqrt{k}}{\partial x_k}\right)^2, \qquad E = 2\frac{\mu\mu_t}{\rho^2}\left(\frac{\partial^2 u}{\partial x_k x_l}\right)^2, \tag{10}$$

where n is the distance from the wall and μ is the laminar viscosity. The eddy viscosity is calculated by

$$\mu_t = \rho f_\mu C_\mu \frac{k^2}{\epsilon}, \tag{11}$$

and the damping functions f_1, f_2 and f_μ are calculated from

$$f_1 = 1, \qquad f_2 = 1 - 0.3\mathrm{e}^{-Re_t^2}, \qquad f_\mu = \mathrm{e}^{-3.4/(1+Re_t/50)^2}, \qquad Re_t = \frac{\rho k^2}{\mu\tilde{\epsilon}}. \tag{12}$$

The closure coefficients take the values

$$C_{\epsilon_1} = 1.44, \quad C_{\epsilon_2} = 1.92, \quad C_\mu = 0.09, \quad \sigma_k = 1.0, \quad \sigma_\epsilon = 1.3. \tag{13}$$

According to this model, the wall boundary conditions for k and ϵ are

$$k_w = 0, \qquad \epsilon_w = \epsilon_0. \tag{14}$$

To improve the model predictions in separated flows, the so-called Yap-correction term [3], YC, has been included in the ϵ-equation

$$YC = 0.83 \frac{\tilde{\epsilon}^2}{k} \left(\frac{l}{c_l y} - 1 \right) \left(\frac{l}{c_l y} \right)^2, \tag{15}$$

where l is the turbulence length scale and $c_l = 0.089$.

The k–ω model [6] has also been employed and the source term, in this case H_ω, is written as

$$H_\omega = J \begin{pmatrix} 0 \\ 0 \\ 0 \\ 0 \\ \tau_{ij}^R \dfrac{\partial u_i}{\partial x_j} - \beta^* \rho \omega k \\ \dfrac{\alpha \omega}{k} \tau_{ij}^R \dfrac{\partial u_i}{\partial x_j} - \beta \rho \omega^2 \end{pmatrix}. \tag{16}$$

The turbulent viscosity is calculated by

$$\mu_t = \alpha^* \frac{\rho k}{\omega}, \tag{17}$$

while the model's coefficients are

$$\beta = \frac{3}{40}, \quad \beta^* = \frac{9}{100}, \quad \alpha = \frac{5}{9}, \quad \alpha^* = 1, \quad \sigma_k = 2, \quad \sigma_\omega = 2. \tag{18}$$

The wall boundary conditions for k and ω are

$$k_w = 0, \qquad \omega_w = \frac{19}{9} \frac{v_w}{\beta y_1^2}, \tag{19}$$

where y_1 is the distance from the wall of the first grid point.

2.3. Characteristics-based method for turbulent flows

The characteristics-based method is a linear Riemann solver for the calculation of the conservative variables along the characteristics (see Figure 1). This method was first presented by Eberle [24] for the compressible Euler equations and was extended by Drikakis *et al.* [25,26] to solve the incompressible Navier–Stokes equations. The inviscid equations are split into two one-dimensional equations.

$$U_t = A_{\text{inv}} U_\xi = 0, \qquad U_t + C_{\text{inv}} U_\zeta = 0. \tag{20}$$

The above equations are used to obtain algebraic relationships for the conservative variables as functions of their values on the characteristics. In this paper, only the extensions of the method due to the incorporation of the convection terms of the turbulence transport equations are presented. For more details on the discretization of the inviscid fluxes of the incompressible and compressible Navier–Stokes equations, the reader is referred to References [24–26].

Following Eberle [20,24], the system of the one-dimensional equations can be expanded in terms of the non-conservative variables ρ, u, w, p, k, ϕ. In this expansion, the characteristic values (denoted below by the subscript l) are also introduced.

The use of the non-conservative variables was chosen because it simplifies the derivation of the expanded form of the one-dimensional equations. The expanded form can be written as

$$\begin{aligned}
&\frac{J}{\Delta t\sqrt{\xi_x^2+\xi_z^2}}(\rho-\rho_l)+(\lambda_0-\lambda)\rho_\xi+\rho(Xu_\xi+Zw_\xi)=0\\
&\rho\left[\frac{J}{\Delta t\sqrt{\xi_x^2+\xi_z^2}}(u-u_l)+(\lambda_0-\lambda)u_\xi\right]+Xp_\xi=0\\
&\rho\left[\frac{J}{\Delta t\sqrt{\xi_x^2+\xi_z^2}}(w-w_l)+(\lambda_0-\lambda)w_\xi\right]+Zp_\xi=0\\
&\frac{J}{\Delta t\sqrt{\xi_x^2+\xi_z^2}}(p-p_l)+(\lambda_0-\lambda)p_\xi+s^2\rho(Xu_\xi+Zw_\xi)=0\\
&\rho\left[\frac{J}{\Delta t\sqrt{\xi_x^2+\xi_z^2}}(k-k_l)+(\lambda_0-\lambda)k_\xi\right]=0\\
&\rho\left[\frac{J}{\Delta t\sqrt{\xi_x^2+\xi_z^2}}(\phi-\phi_l)+(\lambda_0-\lambda)\phi_\xi\right]=0
\end{aligned} \tag{21}$$

where

$$X=\frac{\xi_x}{\sqrt{(\xi_x^2+\xi_z^2)}},\qquad Z=\frac{\zeta_z}{\sqrt{\xi_x^2+\xi_z^2}}, \tag{22}$$

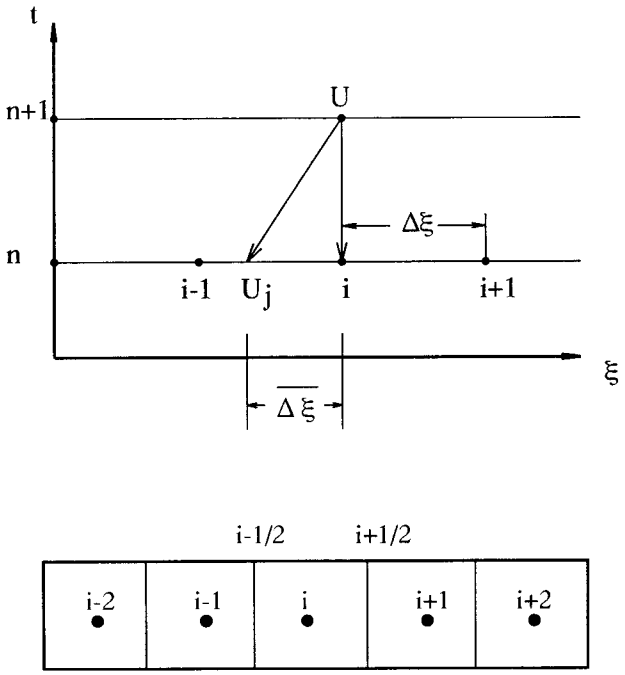

Figure 1. Schematic representation of the one-dimensional characteristic flux extrapolation and control volume notation.

and the eigenvalues λ_0, λ_1 and λ_2 are defined as

$$\lambda_0 = uX + wZ, \qquad \lambda_1 = \lambda_0 + s, \qquad \lambda_2 = \lambda_0 - s, \tag{23}$$

where s is the speed of sound. Similar to the case of the Euler equations [20,24], the following formulae can be derived for the quadruple eigenvalue λ_0

$$\begin{aligned} (p - p_0) - s^2(\rho - \rho_0) &= 0 \\ (w - w_0)X - (u - u_0)Z &= 0 \\ k &= k_0 \\ \phi &= \phi_0 \end{aligned} \tag{24}$$

and for the eigenvalues λ_1 and λ_2

$$\begin{aligned} (p - p_0) + \rho s[Z(u - u_1) + X(w - w_1)] &= 0 \\ (p - p_0) + \rho s[Z(u - u_2) + X(w - w_2)] &= 0 \end{aligned}. \tag{25}$$

Equations (24) and (25) are transformed into the conservative variables using the following formulae

$$\begin{aligned} \Delta u_j &= \frac{\Delta l_j - u\Delta\rho_j}{\rho_j}, \qquad \Delta w_j = \frac{\Delta \eta_j - w\Delta\rho_j}{\rho_j}, \\ \Delta p_j &= (\gamma - 1)\left[\Delta e_j + \frac{(u^2 + w^2)}{2}\Delta\rho_j - u\Delta l_j - w\Delta\eta_j - \Delta m_j\right], \\ \Delta k_j &= \frac{\Delta m_j - k\Delta\rho_j}{\rho_j}, \qquad \Delta\phi_j = \frac{\Delta r_j - \phi\Delta\rho_j}{\rho_j}, \end{aligned} \tag{26}$$

where

$$l_j = (\rho u)_j, \quad \eta_j = (\rho w)_j, \quad m_j = (\rho k)_j, \quad r_j = (\rho\phi)_j, \quad j = 0, 1, 2, \tag{27}$$

and the index j denotes the three characteristics. After some mathematical operations, the following formulae for the conservative variables are obtained

$$\begin{aligned} \rho &= \rho_0 + R_1 + R_2, \\ l &= l_0 + (u + sX)R_1 + (u - sX)R_2, \\ \eta &= \eta_0 + (w + sZ)R_1 + (w - sZ)R_2, \\ e &= e_0 + (H + s\lambda_0)R_1 + (H - s\lambda_0)R_2, \\ m &= m_0 - kR_1 - kR_2, \\ r &= r_0 - \phi R_1 - \phi R_2, \end{aligned} \tag{28}$$

where H is the enthalpy of the fluid and the terms R_1 and R_2 are given by

$$\begin{aligned} R_1 = \frac{1}{2s^2}\Bigg\{&(\rho_1 - \rho_0)\left[\frac{\gamma - 1}{2}(u^2 + w^2) - s\lambda_0\right] + (l_1 - l_0)[sX - u(\gamma - 1)] \\ &+ (\eta_1 - \eta_0)[sZ - w(\gamma - 1)] + (e_1 - e_0)(\gamma - 1) - (m_1 - m_0)(\gamma - 1)\Bigg\}, \end{aligned} \tag{29}$$

$$\begin{aligned} R_2 = \frac{1}{2s^2}\Bigg\{&(\rho_2 - \rho_0)\left[\frac{\gamma - 1}{2}(u^2 + w^2) + s\lambda_0\right] - (l_2 - l_0)[sX + u(\gamma - 1)] \\ &- (\eta_2 - \eta_0)[sZ + w(\gamma - 1)] + (e_2 - e_0)(\gamma - 1) - (m_2 - m_0)(\gamma - 1)\Bigg\}. \end{aligned} \tag{30}$$

The characteristic values at the cell faces are calculated by a five-point upwind extrapolation scheme [18,24] The relationships in Equation (28) are used for the calculation of the conservative variables at the cell faces and, subsequently, for the discretization of the inviscid fluxes.

2.4. Implicit unfactored method

The time integration of the Navier–Stokes and turbulence model equations is obtained by an implicit unfactored method [15] which allows high CFL numbers to be used. The implicit unfactored discretization of the governing equations is combined with Newton subiterations and point-by-point Gauss–Seidel relaxation (IUNGS method) which provides high efficiencies in both vector and parallel computations [21,22].

According to the IUNGS method, Equation (1) is written as

$$\frac{U^{n+1}-U^n}{\Delta t}+E_\xi^{n+1}+G_\zeta^{n+1}=R_\xi^{n+1}+S_\zeta^{n+1}+H_\phi^{n+1}+H_A^{n+1}. \tag{31}$$

The inviscid and viscous fluxes are linearized around the time level n

$$E^{n+1}=E^n+\left(\frac{\partial E}{\partial U}\right)^n\Delta U, \qquad G^{n+1}=G^n+\left(\frac{\partial G}{\partial U}\right)^n\Delta U, \tag{32}$$

$$R^{n+1}=R^n+\left(\frac{\partial R}{\partial U}\right)^n\Delta U, \qquad S^{n+1}=S^n+\left(\frac{\partial S}{\partial U}\right)^n\Delta U, \tag{33}$$

where

$$\Delta U=U^{n+1}-U^n, \tag{34}$$

while the numerical treatment of the source terms is discussed in Section 2.5. Using the above relationships, Equation (31) is written as

$$\frac{\Delta U}{\Delta t}+(A_{\text{inv}}^n\Delta U)_\xi+(C_{\text{inv}}^n\Delta U)_\zeta-(A_{\text{vis}}^n\Delta U)_\xi-(C_{\text{vis}}^n\Delta U)_\zeta+SC=\text{RHS}, \tag{35}$$

where SC are contributions from the linearization of the source terms (see Section 2.5). The right-hand side (RHS) terms are

$$\text{RHS}=-(E_\xi^n+G_\zeta^n-R_\xi^n-S_\zeta^n-H_\phi^n-H_A^n) \tag{36}$$

and

$$A_{\text{inv}}=\frac{\partial E}{\partial U}, \quad C_{\text{inv}}=\frac{\partial G}{\partial U}, \qquad A_{\text{vis}}=\frac{\partial R}{\partial U}, \quad C_{\text{vis}}=\frac{\partial S}{\partial U} \tag{37}$$

are the Jacobians of the inviscid and viscous fluxes.

A Newton-type method can be obtained if a sequence of approximations[1] q^ν, such that $\lim_{\nu>1} q^\nu \to U^{n+1}$ is defined between two time steps n and $n+1$, respectively. Equation (35) is rewritten as

$$\frac{\Delta q^{\nu+1}}{\Delta t}+(A_{\text{inv}}^n\Delta q)_\xi+(C_{\text{inv}}^n\Delta q)_\zeta-(A_{\text{vis}}^n\Delta q)_\xi-(C_{\text{vis}}^n\Delta q)_\zeta=\frac{U^n-q^\nu}{\Delta t}+\text{RHS}, \tag{38}$$

where

[1] q denotes the conservative solution vector U at each Newton subiteration.

$$q^{v+1} = q^{v} + \Delta q^{v+1}. \tag{39}$$

The superscript v denotes Newton subiterations. On the left-hand side (LHS) of Equation (38), thin-layer viscous Jacobian matrices have been used instead of full ones. Numerical experiments have shown that for steady flows, the number of iterations remains the same if the full Jacobians are used [17,18]. The inviscid Jacobians, A and C, are written in terms of their eigenvector and eigenvalue matrices, e.g.

$$A_{\text{inv}} = T\Lambda T^{-1}, \tag{40}$$

where Λ is the eigenvalue matrix and T, T^{-1} are the left and right eigenvector matrices, respectively. These are 6×6 matrices, including the contributions from the turbulence model equations. The Jacobian and eigenvector matrices are given in the Appendix A. The terms $(A^n_{\text{inv}}\Delta U)_\xi$, $(C^n_{\text{inv}}\Delta U)_\zeta$ and $(A^n_{\text{vis}}\Delta U)_\xi$, $(C^n_{\text{vis}}\Delta U)_\zeta$ are discretized up to second-order of accuracy; e.g. the left-hand side terms in the ξ-direction are discretized as

$$\begin{aligned}(A^n_{\text{inv}}\Delta q)_\xi - (A^n_{\text{vis}}\Delta q)_\xi &= (A^n_{\text{inv}}\Delta q)_{i+1/2,k} - (A^n_{\text{inv}}\Delta q)_{i-1/2,k} \\ &\quad - (A^n_{\text{vis}})_{i,k}(\Delta q_{i-1,k} - 2\Delta q_{i,k} + \Delta q_{i+1,k}),\end{aligned} \tag{41}$$

where the superscript $v+1$ has been dropped from Δq for simplicity. In the above

$$\begin{aligned}(A^n_{\text{inv}}\Delta q)_{i+1/2} &= (T\Lambda^+ T^{-1})_{i+1/2,k}(\Delta q)^+_{i+1/2,k} + (T\Lambda^- T^{-1})_{i+1/2,k}(\Delta q)^-_{i+1/2,k} \\ (A^n_{\text{inv}}\Delta q)_{i-1/2} &= (T\Lambda^+ T^{-1})_{i-1/2,k}(\Delta q)^+_{i-1/2,k} + (T\Lambda^- T^{-1})_{i-1/2,k}(\Delta q)^-_{i-1/2,k},\end{aligned}$$

where $\Lambda^+ = \max(0, \Lambda)$ and $\Lambda^- = \min(0, \Lambda)$ are the diagonal matrices of the positive and negative eigenvalues of A_{inv}, respectively. The differences Δq^+ and Δq^- are defined at the cell faces as

$$\begin{aligned}\Delta q^+_{i+1/2} &= \beta\Delta q_i + (1-\beta)(1.5\Delta q_i - 0.5\Delta q_{i-1}), \quad \Delta q^-_{i+1/2} = \Delta q_{i+1}, \\ \Delta q^-_{i-1/2} &= \beta\Delta q_i + (1-\beta)(1.5\Delta q_i - 0.5\Delta q_{i+1}), \quad \Delta q^+_{i-1/2} = \Delta q_{i-1},\end{aligned} \tag{42}$$

where β is a sensor function defined by the maximum of the eigenvalues at the cell faces. To further improve the efficiency of the implicit solution, Gauss–Seidel relaxation is employed and Equation (38) is written for each computational cell (i, k) as

$$(\text{DIAG})^v_{i,k}\Delta q^{\mu+1,v}_{i,k} = -\omega^*(\text{RHS})^v_{i,k} + (\text{ODIAG})^{\mu,v}_{i,k} + \frac{U^n - q^v}{\Delta t}. \tag{43}$$

$(\text{DIAG})^n_{i,k}$ is a 6×6 matrix including the diagonal elements of the eigenvalue-split inviscid Jacobians, the viscous Jacobians and the term $I/\Delta t$. $(\text{ODIAG})_{i,k}$ includes the off-diagonal elements and is a function of $\Delta U_{i+1,k}$, $\Delta U_{i-1,k}$, $\Delta U_{i,k+1}$, $\Delta U_{i,k-1}$. Four Gauss–Seidel steps ($\mu = 4$) and two Newton subiterations ($v = 2$) are performed. The time step Δt is calculated by

$$\Delta t = \frac{\text{CFL}}{[\max|\lambda_{i,k}|] + 2\dfrac{\mu c_p}{Pr}(\xi_x^2 + \xi_z^2 + \zeta_x^2 + \zeta_z^2)}. \tag{44}$$

The under-relaxation parameter ω^* is used to compensate for the different orders of accuracy between the LHS and the RHS. The values of the underrelaxation parameter are: $\omega^* = 0.3$, 0.6 and 0.1 when the RHS is of third-, second- or first-order of accuracy, respectively. The value of $\omega^* = 0.5$ has been used in this study. The CFL number can take values up to 60 when the implicit-coupled implementation is used.

For multidimensional problems, the matrix $(\text{DIAG})^v_{i,k}$ has zero or negative diagonal elements and is, therefore, ill-posed for Gauss-elimination. To recover high values of the CFL number,

preconditioning is performed on each Gauss–Seidel subiteration [20,24]. The conservative vector Δq is multiplied by the Jacobian, $M = \partial q^*/\partial q$ before the Gauss-elimination

$$(\Delta q)^{*\,\mu+1}_{i,k} = M(\Delta q)^{\mu+1}_{i,k}, \tag{45}$$

where $q^* = (p,\ u,\ w,\ p,\ k,\ \phi)^T$ is the vector of the non-conservative variables. After every Gauss-elimination, the solution is again converted to the vector Δq by multiplication with the matrix $M^{-1} = \partial q/\partial q^*$.

The implicit-coupled implementation can be applied to different versions of the k–ϵ model by changing the damping functions, closure coefficients and boundary conditions only. The Jacobians in the implicit part of the algorithm remain unchanged for all two-equation turbulence models.

2.5. Implicit treatment of the source terms

Considering the equation

$$\frac{\partial U}{\partial t} = H \equiv H(U,\ U_\xi,\ U_\zeta), \tag{46}$$

where

$$U = \begin{pmatrix} \rho k \\ \rho\tilde{\epsilon} \end{pmatrix}, \quad H = \begin{pmatrix} H_k \\ H_{\tilde{\epsilon}} \end{pmatrix}, \tag{47}$$

then the following time discretization can be obtained,

$$U^{n+1} = U^n + \Delta t H^{n+1}. \tag{48}$$

After linearization of the matrix H^{n+1},

$$H^{n+1} = H^n + \frac{\partial H}{\partial U}(U^{n+1} - U^n), \tag{49}$$

Equation (48) can be written as

$$(U^{n+1} - U^n)\left(I - \Delta t \frac{\partial H}{\partial U}\right) = \Delta t H^n. \tag{50}$$

Stability analysis of Equation (46) shows that the implicit discretization (50) is unstable if $H > 0$. Hence, only negative terms can be moved to the LHS of Equation (50) and as a result to the LHS of Equation (43).

For the case of the k–ϵ turbulence model, the negative source terms are of the form

$$H_k = -\rho\tilde{\epsilon}, \qquad H_{\tilde{\epsilon}} = -C_{\epsilon 2} f_2 \frac{(\rho\tilde{\epsilon})^2}{\rho k}. \tag{51}$$

Using the relation $\mu_t = C_\mu f_\mu((\rho k)^2/\rho\tilde{\epsilon})$, the above relations are written as

$$H_k = -c_\mu f_\mu \frac{(\rho k)^2}{\mu_t}, \qquad H_{\tilde{\epsilon}} = -C_{\epsilon 2} f_2 \frac{(\rho\tilde{\epsilon})^2}{(\rho k)}. \tag{52}$$

The Jacobian matrix $\partial H/\partial U$ is given by

$$\frac{\partial H}{\partial U} = \begin{bmatrix} -2\dfrac{C_\mu f_\mu}{\mu_t}(\rho k) & 0 \\ C_{\epsilon 2} f_2 \dfrac{(\rho\tilde{\epsilon})^2}{(\rho k)^2} & -2C_{\epsilon 2} f_2 \dfrac{\rho\tilde{\epsilon}}{\rho k} \end{bmatrix} \tag{53}$$

and its diagonal elements are added to the $(\mathrm{DIAG})^n_{i,k}$ term of Equation (43) in order to increase the diagonal dominance.

The source term accounting for axisymmetric flows is written as

$$H_A = J\left(-\frac{\tilde{G}}{z} + \frac{\tilde{S}^a}{z} + (0, 0, p - \tau_{\theta\theta}, 0, 0, 0)^T \right) + H_A^{\mathrm{extra}}. \tag{54}$$

The matrix $\tilde{S}^a$ is defined similar to the flux $\tilde{S}$ with the only difference being that the components of the stress tensor t_{ij} are expanded to an axisymmetric co-ordinate system. The axisymmetric stress components are given by

$$\begin{aligned} t^a_{xx} &= \mu^*\left(\frac{4}{3}\frac{\partial u}{\partial x} - \frac{2}{3}\frac{\partial w}{\partial z} - \frac{2}{3}\frac{w}{z}\right) - \frac{2}{3}\rho k, \quad t^a_{zz} = \mu^*\left(\frac{4}{3}\frac{\partial w}{\partial z} - \frac{2}{3}\frac{\partial u}{\partial x} - \frac{2}{3}\frac{w}{z}\right) - \frac{2}{3}\rho k, \\ t_{\theta\theta} &= \mu^*\left(\frac{4}{3}\frac{w}{z} - \frac{2}{3}\left(\frac{\partial u}{\partial x} + \frac{\partial w}{\partial z}\right)\right) - \frac{2}{3}\rho k, \quad t^a_{xz} = \mu^*\left(\frac{\partial w}{\partial x} + \frac{\partial u}{\partial z}\right), \end{aligned} \tag{55}$$

where $\mu^* = \mu + \mu_t$. In the computational code, the velocity derivatives are also expanded to curvilinear co-ordinates, e.g.

$$\frac{\partial u}{\partial x} = \frac{\partial u}{\partial \xi}\frac{\partial \xi}{\partial x} + \frac{\partial u}{\partial \zeta}\frac{\partial \zeta}{\partial x}.$$

The above tensor components can also be rewritten using their Cartesian counterparts as

$$\begin{aligned} t^a_{xx} &= t_{xx} + \mu^*\left(-\frac{2}{3}\frac{w}{z}\right), \qquad t^a_{zz} = t_{zz} + \mu^*\left(-\frac{2}{3}\frac{w}{z}\right), \\ t_{\theta\theta} &= \mu^*\left(\frac{4}{3}\frac{w}{z} - \frac{2}{3}\left(\frac{\partial u}{\partial x} + \frac{\partial w}{\partial z}\right)\right), \quad t^a_{xz} = t_{xz} = t_{zx}. \end{aligned} \tag{56}$$

The matrix H_A^{extra} originates from the axisymmetric contribution of the stresses into the viscous fluxes and is considered here separately in order to explain its numerical implementation

$$\begin{aligned} H_A^{\mathrm{extra}} = \frac{\partial}{\partial \xi}\left[J\xi_x \begin{pmatrix} 0 \\ -\frac{2}{3}\frac{w}{z}\mu^* \\ 0 \\ -u\frac{2}{3}\frac{w}{z}\mu^* \\ 0 \\ 0 \end{pmatrix} + J\xi_x \begin{pmatrix} 0 \\ 0 \\ -\frac{2}{3}\frac{w}{z}\mu^* \\ -\frac{2}{3}\frac{w^2}{z}\mu^* \\ 0 \\ 0 \end{pmatrix} \right] \\ + \frac{\partial}{\partial \zeta}\left[J\zeta_x \begin{pmatrix} 0 \\ -\frac{2}{3}\frac{w}{z}\mu^* \\ 0 \\ -u\frac{2}{3}\frac{w}{z}\mu^* \\ 0 \\ 0 \end{pmatrix} + J\zeta_x \begin{pmatrix} 0 \\ 0 \\ -\frac{2}{3}\frac{w}{z}\mu^* \\ -\frac{2}{3}\frac{w^2}{z}\mu^* \\ 0 \\ 0 \end{pmatrix} \right]. \end{aligned} \tag{57}$$

The term H_A can also be written as

$$H_A = H_A^{\mathrm{inv}} + H_A^{\mathrm{vis}} + H_A^{\mathrm{extra}}, \tag{58}$$

where

$$H_A^{\text{inv}} = -\frac{J}{z}\begin{pmatrix} \rho w \\ \rho uw \\ \rho w^2 + p \\ (e+p)w \\ \rho wk \\ \rho w\phi \end{pmatrix}, \quad H_A^{\text{vis}} = \frac{J}{z}\begin{pmatrix} 0 \\ t_{xz} \\ t_{zz} - t_{\theta\theta} - \frac{2}{3}\mu^* \frac{w}{z} \\ (ut_{xz} + wt_{zz} - \dot{q}_z) - \frac{2}{3}\mu^* \frac{w^2}{z} \\ \left(\mu + \frac{\mu_t}{\sigma_k}\right)\frac{\partial k}{\partial z} \\ \left(\mu + \frac{\mu_t}{\sigma_\phi}\right)\frac{\partial \phi}{\partial z} \end{pmatrix}. \tag{59}$$

The terms H_A^{inv} and H_A^{vis} are linearized, similar to the fluxes, around the time level $n+1$

$$(H_A^{\text{inv}})^{n+1} = (H_A^{\text{inv}})^n + \frac{\partial H_A^{\text{inv}}}{\partial U}(U^{n+1} - U^n), \tag{60}$$

$$(H_A^{\text{vis}})^{n+1} = (H_A^{\text{vis}})^n + \frac{\partial H_A^{\text{vis}}}{\partial U}(U^{n+1} - U^n). \tag{61}$$

The Jacobians $\partial H_A^{\text{inv}}/\partial U$ and $\partial H_A^{\text{vis}}/\partial U$ are defined on the centroids (i,k), and therefore, contribute to the diagonal elements $(\text{DIAG})_{i,k}^{\nu}$ of the matrix inversion in Equation (43). If the term H_A^{extra} had also been linearized, then, due to the presence of spatial derivatives in Equation (57), the elements of the Jacobian $\partial H_A^{\text{extra}}/\partial U$ would contribute only to the off-diagonal elements, $(\text{ODIAG})_{i,k}^{\mu,\nu}$, of the matrix inversion in Equation (43). Therefore, in the present study, the term H_A^{extra} was not linearized and was simply added as source to the RHS (Equation (36)).

Moreover, it was found that the implicit treatment of the axisymmetric terms only slightly influences the numerical convergence. Therefore, the additional CPU time required to compute and add these terms to the diagonal elements $(\text{DIAG})_{i,k}^{n}$ balances the slight reduction, if any at all, in the number of iterations. There is a fundamental difference between the treatment of the sources for the turbulence model and those due to the axisymmetric formulation. Turbulence model source terms are mainly responsible for the stiffness of the final system of equations. This is the reason why linearization of these terms was found to have a positive influence on the rate of convergence. The source terms due to the axisymmetric formulation have small values on the LHS (zero for planar cases) and, subsequently, have no significant influence on the performance of the implicit method.

2.6. *Implicit-coupled, implicit-decoupled and explicit strategies*

The objective of the present work is to extend an implicit unfactored method to the coupled solution of the low-*Re* model and Navier–Stokes equations. This method is henceforth labeled *implicit-coupled* scheme. The efficiency of this method is verified in contrast to *implicit-decoupled* and *explicit schemes*.

In the *implicit-decoupled* scheme, the implicit solution is only used for the fluid-flow equations, while the turbulent transport equations are solved by the Runge–Kutta explicit scheme. Furthermore, one may adopt the Runge–Kutta scheme to solve both the fluid-flow and turbulent-flow equations. This third alternative will henceforth be labeled *explicit-scheme*.

In the present work, the Launder–Sharma k–ϵ and the k–ω models have been implemented in conjunction with the implicit and explicit solution procedures.

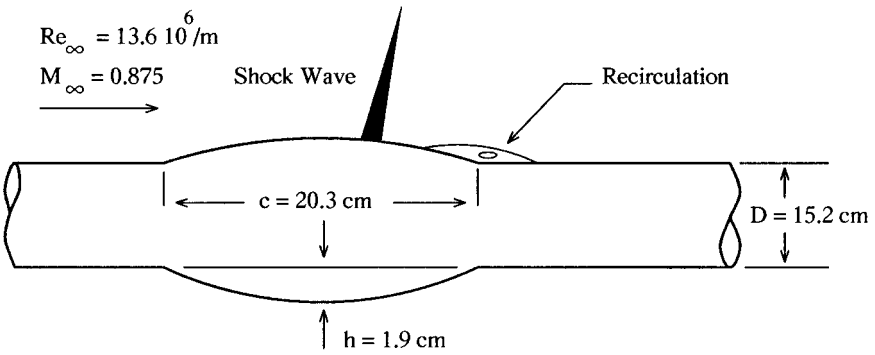

Figure 2. Schematic for the axisymmetric bump geometry.

3. RESULTS

3.1. Description of the flow case

The flow over an axisymmetric bump geometry (Figure 2) has been selected for the validation of the implicit method and turbulence models. For this geometry, experimental measurements for the wall pressure distribution, as well as the velocity, turbulent shear stress and turbulent kinetic energy profiles at various x/c locations, have been performed by Johnson *et al.* [27]. Furthermore, numerical results have been reported by other researchers [12,18,27] using different computational methods and turbulence models than the present ones.

The experimental results by Johnson *et al.* [27] correspond to $M_\infty = 0.875$ and Reynolds number per unit length, $Re\ \mathrm{m}^{-1} = 13.6 \times 10^6\ \mathrm{m}^{-1}$. All lengths have been non-dimensionalized using the bump's length, c.

Three computational grids, 40×20, 80×40 and 160×80, respectively, have been used and details for these grids are given in Table I. The second grid (G2) is comparable with that used by Sahu and Danberg [12]. The third grid (G3) is similar to that used by Drikakis and Durst [18]. The grids G2 and G3 correspond to $y^+ \simeq 0.5$ and $y^+ \simeq 0.1$, respectively. A partial view of the finest grid is shown in Figure 3. The third grid was sufficient to obtain a grid-independent solution.

3.2. Implicit-coupled versus implicit-decoupled and explicit schemes

The convergence histories for the conservative variables are shown in Figure 4 for the k–ϵ and k–ω models using the implicit-coupled method and the finest grid. All results were obtained on a HP 9000/735/99 workstation using double precision computer arithmetics.

Table I. Finite volume grids used in the calculation

Grid	Computational volumes	Minimum and maximum x-co-ordinates	Minimum and maximum z-co-ordinates	Distance from the wall of the first grid node
G1	40×20	$-5/5$	3.4/4	5×10^{-5}
G2	80×40	$-5/6$	3.4/4	1×10^{-5}
G3	160×80	$-6/6$	3.4/4	1×10^{-6}

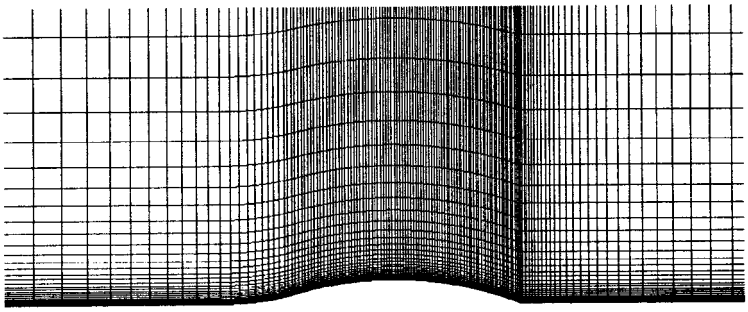

Figure 3. Partial view of the finest computational grid (G3).

About 500 work-units (one work-unit represents a minute of CPU time) are needed to reduce the norm of error less than 10^{-4} with the implicit-coupled solver and the $k-\omega$ model. In these Figures, the maximum normalized changes of the conservative variables are plotted. The $k-\omega$ model requires less work-units than the $k-\epsilon$ model to obtain the steady state solution. The different convergence behavior between the two models is due to the boundary condition for ω. Wilcox [7] reported that the boundary condition for ω has a stabilizing effect on the convergence of numerical schemes.

Figure 5 compares the convergence of the implicit-coupled strategy with the implicit-decoupled and explicit schemes. The maximum error in the sum of all fluxes over all computational cells is used as an indicator of convergence. For both turbulence models, one may see that the implicit-coupled solution requires less work-units than the explicit scheme and almost half of the work-units of the implicit-decoupled solution.

The work-units required for a steady state solution using different solution strategies are presented in Table II. From this table, one can see that the efficiency of the implicit-coupled solver is greater than that of other schemes. Even though at each time step the implicit solution requires extra computing effort to invert the 6×6 system of equations, less iterations are required in comparison with the implicit-decoupled and explicit schemes. The work-units required for the solution of the same problem using the Baldwin–Lomax algebraic turbulence model are also given. The solution using low-*Re* two-equation turbulence models requires almost double the work-units.

3.3. Comparison with experimental data and numerical solutions

Results for the shock wave location are given in Table III. The prediction of the shock location using the Launder–Sharma $k-\epsilon$ model are closer to the experimental results by Johnson *et al.* [27] as well as the numerical predictions of previous studies [12,18]. The $k-\omega$ model shifted the shock location upstream. The same behavior was also reported by Johnson *et al.* [27] in their numerical calculations with the $k-\omega$ model.

Calculations using three computational grids were carried out in order to verify the grid-independent solution. Large differences were found between the grids G1 and G2. Comparison of the surface pressure distribution on grids G2 and G3 are shown in Figures 6 and 7 for the $k-\epsilon$ and $k-\omega$ models, respectively. Calculations using finer grids showed that G3 is sufficient to obtain a grid-independent solution.

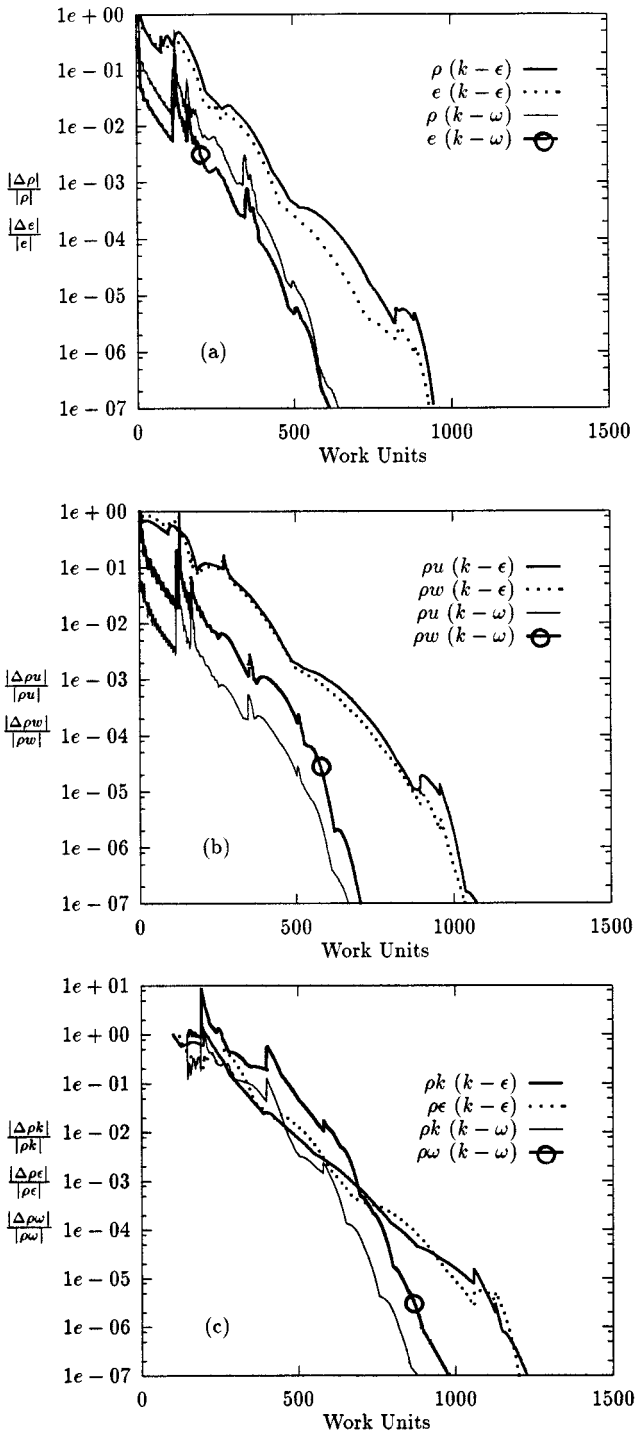

Figure 4. Convergence histories for the Launder–Sharma k–ϵ and k–ω models using the grid G3: (a) density and energy, (b) velocity components, (c) ρk, $\rho\epsilon$ and $\rho\omega$.

The surface pressure distributions obtained by the k–ϵ and k–ω models were compared with the numerical results by Sahu and Danberg [12] and Liou and Shih [11], as well as with experimental data by Johnson *et al.* [27]. The comparisons are shown in Figures 6 and 7 for the k–ϵ and the k–ω models, respectively. Better results are obtained using the Launder–Sharma k–ϵ model, while the k–ω model seems to overestimate the pressure values downstream of the shock. The present results are in better agreement with the experimental than the numerical predictions obtained in References [11,12] using Chien's k–ϵ turbulence model.

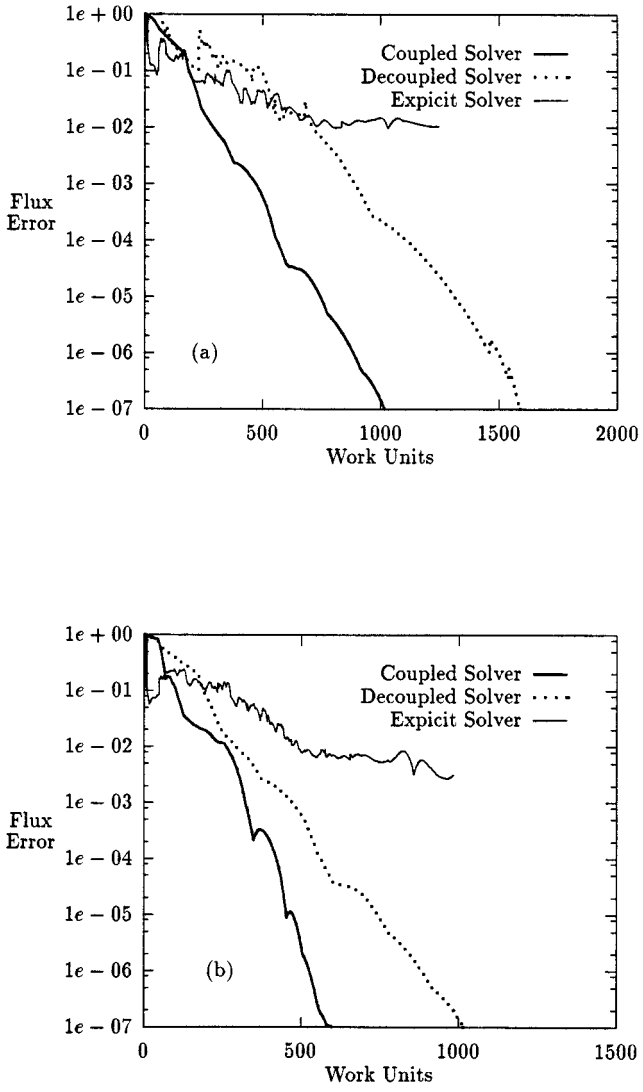

Figure 5. Convergence histories (on grid G3) for (a) the Launder–Sharma k–ϵ model, and (b) the k–ω model, using the implicit-coupled, implicit-decoupled and explicit schemes.

Table II. Work-units for steady state solution using the $k-\omega$ model[a]

Grid	Implicit-coupled	Implicit-decoupled	Explicit
G1	51.7 (10.8)	60.48	76.9
G2	163.2 (105.0)	436.8	661.05
G3	971.1 (616.5)	1792.7	8597.2

[a] Numbers in brackets refer to the calculation with the Baldwin–Lomax algebraic turbulence model.

Table III. Comparisons between present results, experimental data by Johnson *et al.* [27] and past numerical results [12,18], for the shock-wave location

Reference	Shock position x/c	Turbulence model
Experiment	$\simeq 0.7$	
Present work (grid G3)	0.70	Launder–Sharma $k-\epsilon$
Present work (grid G3)	0.65	$k-\omega$
Drikakis and Durst	0.69	Baldwin–Lomax
Sahu and Danberg	0.7	Chien's $k-\epsilon$

Comparisons with the experimental results for the velocity, turbulent kinetic energy and turbulent shear stress profiles are given in Figure 8. The velocity predictions are better for the $k-\epsilon$ model (Figure 8). For both models, the predictions of the turbulent shear stress show reasonable trends only upstream and downstream of the shock. Large discrepancies occur in the region near the shock wave. Comparing the results of the two models (Figure 8), it is not obvious which model gives the best results for the turbulent shear stress. The results for the turbulent kinetic energy (Figure 8) show again that in the regions where no separation occurs, the predictions are in better agreement with the experimental data. Past numerical studies using different models and methods have revealed the same behavior [12,18].

4. CONCLUSIONS

Implicit unfactored implementation of low-*Re* two-equation turbulence models in conjunction with a characteristics-based method for compressible flows was presented. The validation of the method has been obtained by comparisons with experimental and numerical results appearing in the literature. The present method has also been assessed in contrast to decoupled and explicit solution strategies. The implicit unfactored method has been applied for both the $k-\epsilon$ and $k-\omega$ models. From this study the following conclusions can be drawn:

1. The coupling of two-equation turbulence models with the Navier–Stokes equations using the present implicit unfactored scheme results in robust numerical solutions in turbulent compressible flows. The implicit coupling of the turbulence model and Navier–Stokes equations results in more efficient solutions compared with the implicit-decoupled and explicit ones.
2. Little effort and minor modifications are required to implement other versions of the $k-\epsilon$ or $k-\omega$ models in the existing implicit-coupled solver.
3. The Launder–Sharma $k-\epsilon$ model with the Yap-correction predicts better the boundary layer separation than the $k-\omega$ model. However, different versions [7,8,28] of the $k-\omega$ model have also to be investigated in order to confirm this conclusion.

4. The calculations showed that the $k-\omega$ model gives faster solutions than the Launder–Sharma $k-\epsilon$ model.

The extension of the implicit method in conjunction with Reynolds stress and non-linear eddy viscosity models for both steady and unsteady flows, is in progress and results will be presented in a future paper.

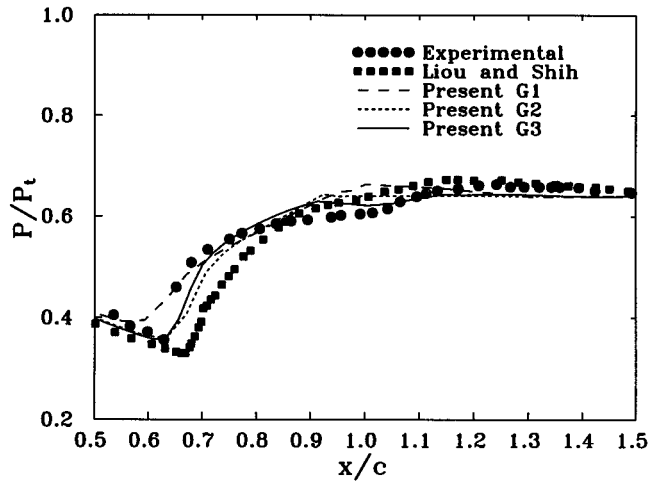

Figure 6. Comparison between the present results using the Launder–Sharma $k-\epsilon$ model, the experiments by Johnson *et al.* [27] and simulation results by Liou and Shih [11] for the surface pressure distribution over the axisymmetric bump.

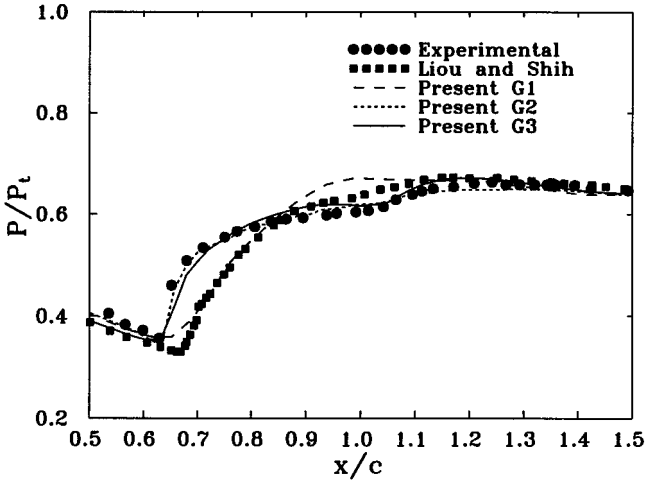

Figure 7. Comparison between present results using the $k-\omega$ model, experiments by Johnson *et al.* [27] and simulation results by Liou and Shih [11] for the surface pressure distribution over the axisymmetric bump.

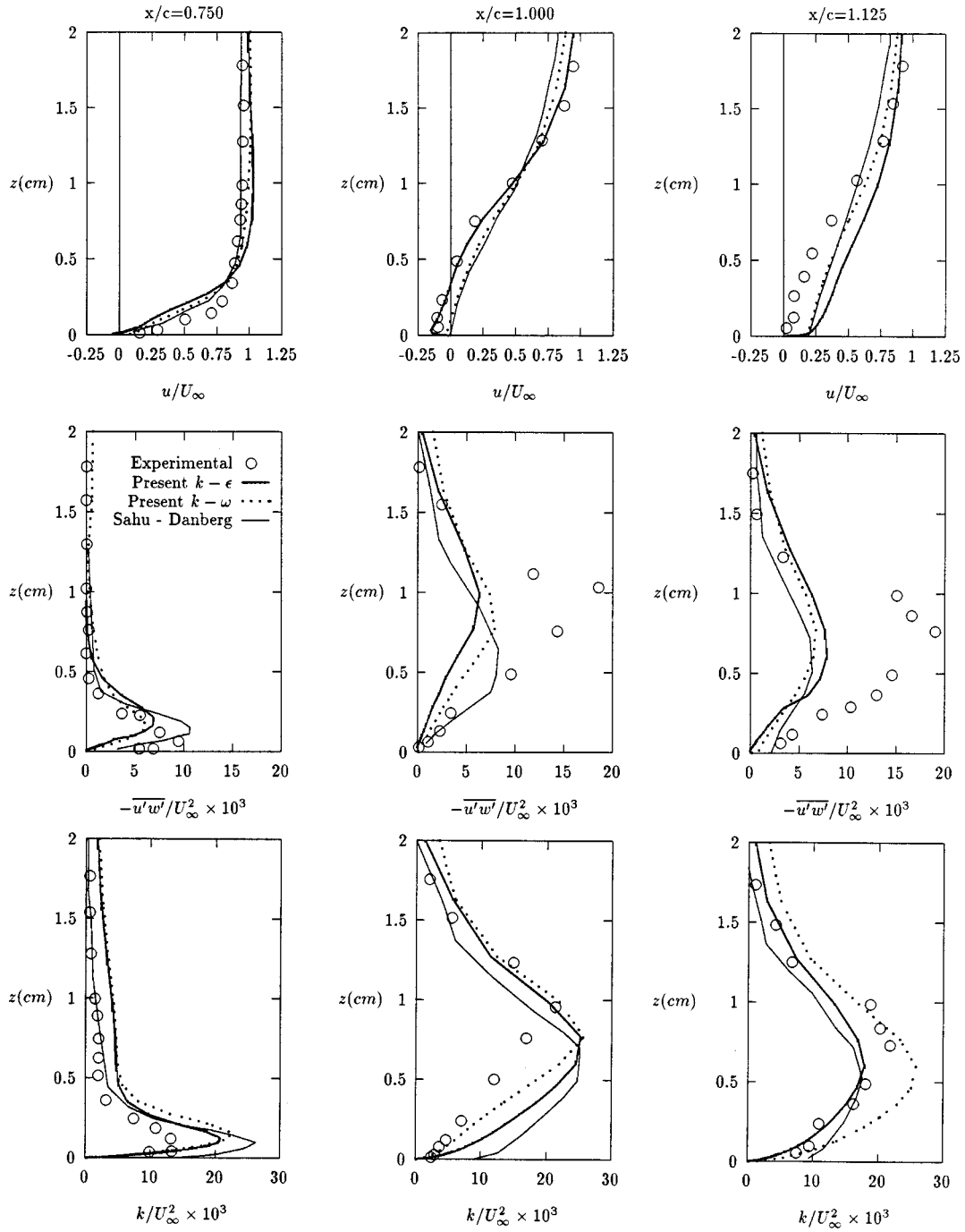

Figure 8. Comparison between present results, experiments by Johnson *et al.* [27] and computations by Sahu and Danberg [12] for the velocity, turbulent shear stress and turbulent kinetic energy profiles.

ACKNOWLEDGMENTS

Financial support from CEC through the COP-94-1239 project is gratefully acknowledged. The authors would like to thank Professor M.A. Leschziner and Drs U. Goldberg and P. Batten for several discussions during the preparation of this work. The authors also thank UMIST and National Technical University of Athens (through the 'L. Economides' scholarship) for additional financial support.

APPENDIX A. JACOBIANS OF THE INVISCID FLUXES

The Jacobian matrices of the inviscid fluxes E and G are given by

$$A=\frac{\partial E}{\partial U}=J\left(\frac{\partial \tilde{E}}{\partial U}\xi_x+\frac{\partial \tilde{G}}{\partial U}\xi_z\right), \tag{62}$$

$$C=\frac{\partial G}{\partial U}=J\left(\frac{\partial \tilde{E}}{\partial U}\zeta_x+\frac{\partial \tilde{G}}{\partial U}\zeta_z\right). \tag{63}$$

The Jacobian $\tilde{A}=\partial\tilde{E}/\partial U$ of the Cartesian flux $\tilde{E}$, as well as the corresponding eigenvector matrices $\tilde{T}$ and $\tilde{T}^{-1}$ are given below

$$\tilde{A}=\begin{pmatrix} 0 & 1 & 0 & 0 & 0 & 0 \\ Q(\gamma-1)-u^2 & (3-\gamma)u & -(\gamma-1)u & \gamma-1 & \left(\frac{5}{3}-\gamma\right) & 0 \\ -uw & w & u & 0 & 0 & 0 \\ \tilde{A}_{41} & \tilde{A}_{42} & -(\gamma-1)uw & \gamma u & \left(\frac{5}{3}-\gamma\right)u & 0 \\ -uk & k & 0 & 0 & u & 0 \\ -u\tilde{\epsilon} & \tilde{\epsilon} & 0 & 0 & 0 & u \end{pmatrix}, \tag{64}$$

where

$$\tilde{A}_{41}=2(\gamma-1)Qu-uk\left(\frac{5}{3}-\gamma\right)-\gamma\frac{eu}{\rho} \tag{65}$$

and

$$\tilde{A}_{42}=\left(\frac{\gamma-1}{\rho}\right)+k\left(\frac{5}{3}-\gamma\right)-(\gamma-1)\left(\frac{3u^2+w^2}{2}\right). \tag{66}$$

The eigenvector matrix $\tilde{T}$ is

$$\tilde{T}=\begin{pmatrix} 1-\frac{Q(\gamma-1)}{s^2} & \frac{(\gamma-1)u}{s^2} & \frac{(\gamma-1)w}{s^2} & -\frac{\gamma-1}{s^2} & -\frac{1}{s^2}\left(\frac{5}{3}-\gamma\right) & 0 \\ -us+Q(\gamma-1) & s-(\gamma-1)u & -(\gamma-1)w & \gamma-1 & (5/3)-\gamma & 0 \\ -\frac{w}{\rho} & 0 & \frac{1}{\rho} & 0 & 0 & 0 \\ us+Q(\gamma-1) & -s-(\gamma-1)u & -(\gamma-1)w & \gamma & \left(\frac{5}{3}-\gamma\right) & 0 \\ -\frac{k}{\rho} & 0 & 0 & 0 & \frac{1}{\rho} & 0 \\ -\frac{\tilde{\epsilon}}{\rho} & 0 & 0 & 0 & 0 & \frac{1}{\rho} \end{pmatrix} \tag{67}$$

and $\tilde{T}^{-1}$ is

$$\tilde{T}^{-1}=\begin{pmatrix} 1 & \frac{1}{2s^2} & 0 & \frac{1}{2s^2} & 0 & 0 \\ u & \frac{u}{2s^2}+\frac{1}{2s} & 0 & \frac{u}{2s^2}-\frac{1}{2s} & 0 & 0 \\ w & w/(2s^2) & \rho & w/(2s^2) & 0 & 0 \\ \tilde{T}_{41}^{-1} & \tilde{T}_{42}^{-1} & \rho w & \tilde{T}_{44}^{-1} & \tilde{T}_{45}^{-1} & 0 \\ k & \frac{k}{2s^2} & 0 & \frac{k}{2s^2} & \rho & 0 \\ \tilde{\epsilon} & \frac{\tilde{\epsilon}}{2s^2} & 0 & \frac{\tilde{\epsilon}}{2s^2} & 0 & \rho \end{pmatrix}, \tag{68}$$

where

$$\tilde{T}_{41}^{-1}=Q+\frac{k}{\gamma-1}\left(\frac{5}{3}-\gamma\right), \tag{69}$$

$$\tilde{T}_{42}^{-1}=\frac{Q}{2s^2}-\frac{k}{2(\gamma-1)s^2}\left(\frac{5}{3}-\gamma\right)+\frac{u}{2s}+\frac{1}{2(\gamma-1)}, \tag{70}$$

$$\tilde{T}_{44}^{-1}=\frac{Q}{2s^2}-\frac{k}{2(\gamma-1)s^2}\left(\frac{5}{3}-\gamma\right)+\frac{u}{2s}+\frac{1}{2(\gamma-1)}, \tag{71}$$

$$\tilde{T}_{45}^{-1}=-\frac{\rho}{\gamma-1}\left(\frac{5}{3}-\gamma\right), \tag{72}$$

and s is the speed of sound, which for an ideal gas is given by

$$s=\sqrt{\frac{\gamma p}{\rho}}, \tag{73}$$

Q is the kinetic energy of the fluid per unit mass

$$Q=\frac{u^2+w^2}{2}. \tag{74}$$

Similar relations can be extracted for the Jacobian $\tilde{C}$.

REFERENCES

1. B.E. Launder and D.B. Spalding, 'The numerical computation of turbulent flows', *Comput. Methods Appl. Mech. Eng.* **3**, 269–289 (1974).
2. W.P. Jones and B.E. Launder, 'The prediction of laminarization with a two-equation model of turbulence', *Int. J. Heat Mass Transf.* **15**, 301–314 (1972).
3. C.R. Yap, 'Turbulent heat and momentum transfer in recirculating and impinging flows', *Ph.D Thesis*, Faculty of Technology, UMIST, 1987.
4. B.E. Launder and B.I. Sharma, 'Application of the energy-dissipation model of turbulence to the calculation of flow near a spinning disk', *Lett. Heat Mass Transf.* **1**, 131–138 (1974).
5. K.-Y. Chien, 'Predictions of channel and boundary layer flows with a low-Reynolds number turbulence model', *AIAA J.* **20**, 33–38 (1992).
6. D.C. Wilcox and R.M. Traci, 'A complete model of turbulence', *AIAA Paper* 76-351, July, 1976.
7. D.C. Wilcox, *Turbulence Modeling for CFD*, DCW Industries, Wilcox, CA, 1993.

8. F.R. Menter, 'Influence of freestream values on $k-\omega$ turbulence model predictions', *AIAA J.* **30**, 1657–1659 (1992).
9. F. Liu, 'Multigrid solution of the Navier–Stokes equations with a two-equation turbulence model', in D.A. Caughey and M.M. Hafez (eds.), *Frontiers of Computational Fluid Dynamics*, Wiley, New York, 1994, pp. 339–359.
10. R.F. Kunz and B. Lakshminarayama, 'Explicit Navier–Stokes computation of cascade flows using the $k-\epsilon$ turbulence model', *AIAA J.* **30**, 13–22 (1992).
11. W.W. Liou and T.H. Shih, 'Transonic turbulent flow predictions with two-equation turbulence models', ICOMP, NASA, Lewis, CR, 1996.
12. J. Sahu and J. Danberg, 'Navier–Stokes computations of transonic flows with a two-equation turbulence model', *AIAA J.* **24**, 1744–1751 (1986).
13. G.A. Gerolymos and I. Vallet, 'Implicit computation of three-dimensional compressible Navier–Stokes equations using $k-\epsilon$ closure', *AIAA J.* **34**, 1321–1330 (1996).
14. H. Lin, D.Y. Yang and C.-C. Chieng, 'Variants of biconjugate gradient method for compressible Navier–Stokes solver', *AIAA J.* **33**, 1177–1184 (1995).
15. S.R. Chakravarthy, 'High resolution upwind formulations for the Navier–Stokes equations', *VKI Lecture Series*, *Computational Fluid Dynamics*, 1988-05, 1988.
16. A. Eberle, '3D Euler calculations using characteristic flux extrapolation', *AIAA-85-0119*, January 14–17, Reno, NV, 1985.
17. M.A. Schmatz, A. Brenneis and A. Eberle, 'Verification of an implicit relaxation method for steady and unsteady viscous flow problems', *AGARD CP 437*, 15-1–33, 1988.
18. D. Drikakis and F. Durst, 'Investigation of flux formulae in transonic shock wave/turbulent boundary layer interaction', *Int. J. Numer. Methods Fluids* **18**, 385–413 (1994).
19. J.P. Chen and D.L. Whitfield, 'Navier–Stokes calculations for the unsteady flow-field of turbomachinery', *AIAA-93-0676*, *31st Aerosp. Sci. Meet.*, January 11–14, Reno, NV, 1993.
20. A. Eberle, A. Rizzi and E.H. Hirschel, Numerical Solutions of the Euler Equations for Steady Flow Problems, *Notes Numerical Fluid Mechanics*, vol. 34, Wiesbaden, Vieweg-Verlag, 1992.
21. D. Drikakis, E. Schreck and F. Durst, 'Performance analysis of viscous flow computations on various parallel architectures', *ASME J. Fluids Eng.* **116**, 835–841 (1994).
22. D. Drikakis and F. Durst, 'Parallelization of inviscid and viscous flow solvers', *Int. J. Comput. Fluid Dyn.* **3**, 101–121 (1994).
23. R. Peyret and H. Viviand, 'Computation of viscous compressible flows based on the Navier–Stokes equations', *AGARD AG-212 Rep.*, 1975.
24. A. Eberle, 'Characteristic flux averaging approach to the solution of Euler's equations', *VKI Lecture Series*, *Computational Fluid Dynamics 1987-04*, 1987.
25. D. Drikakis, P.A. Govatsos and D.E. Papantonis, 'A characteristics-based method for incompressible flows', *Int. J. Numer. Methods Fluids* **19**, 667–685 (1994).
26. D. Drikakis, 'A parallel multiblock characteristics-based method for 3D incompressible flows', *Adv. Eng. Softw.* **26**, 111-119 (1996).
27. D.A. Johnson, C.C. Horstman and W.D. Bachalo, 'Comparison between experiment and prediction for a transonic turbulent separated flow', *AIAA J.* **20**, 737–744 (1982).
28. Menter F.R., 'Two-equation eddy-viscosity turbulence models for engineering applications', *AIAA J.* **32**, 57–63 (1994).

